Journal of Materials Research and Technology 34 (2025) 1265–1274

Contents lists available at ScienceDirect

Journal of Materials Research and Technology

journal homepage: www.elsevier.com/locate/jmrt

Enhancing mechanical properties of $(HfMoNbZrTa)_{1-x}N_x$ films through multi-phase structures in substoichiometric compositions

Yiming Ruan [a], Jigang Xie [a], Lin He [a], Fugui Zhang [a], Jie Shi [b], Hengning Hu [b], Yun Chen [b], Rui Shu [c], Liuquan Yang [d], Hao Du [a,e,*]

[a] School of Mechanical Engineering, Guizhou University, Guiyang, 550025, PR China
[b] Chengdu Tool Research Institute CO., Ltd., Chengdu, 610500, PR China
[c] Department of Science and Technology, Linköping University, SE-60174, Norrköping, Sweden
[d] School of Mechanical Engineering, University of Leeds, Leeds, LS2 9JT, UK
[e] State Key Laboratory of Public Big Data, Guizhou University, Guiyang, 550025, PR China

ARTICLE INFO

Keywords:
Multi-principal element nitrides
Density functional theory
Multi-phase structure
Local lattice distortion

ABSTRACT

Elemental composition design is a common strategy for tuning the crystallographic structure of films, thereby optimizing their mechanical properties. The evolution of film structure is highly dependent on both selection and concentration of cation and anion elements. In this work, we utilized strong nitride-forming elements (Hf, Nb, Zr, and Ta) and the weak nitride-forming element Mo as the metallic cations in a multi-principal element nitride system. The nitrogen content in the $(HfMoNbZrTa)_{1-x}N_x$ film was manipulated by varying the N_2/Ar flow ratio (R_N) during reactive magnetron sputtering. The results showed that the HfMoNbZrTa metallic film crystallized weakly into a body-centered cubic (BCC) structure, yielding a hardness (H) of approximately 10.7 ± 0.2 GPa. The incorporation of nitrogen immediately induced a transformation from BCC to a face-centered cubic (FCC) predominated multi-phase structure at substoichiometric regimes (10% ≤ R_N ≤ 20%). A further increase of R_N to ≥25%, i.e., at near-stoichiometric regimes, resulted in the formation of single-phase FCC structure. Hardness and wear rates both reached their optimal values at R_N = 20–25%. The strengthening mechanism was elucidated through density functional theory (DFT) calculations, which suggest that higher H of the substoichiometric film is mainly associated with the increased local lattice distortion and the formation of a multi-phase structure.

1. Introduction

The transition metal nitrides (TMNs) with TM in groups of IVB, VB and VIB (TM = Ti, Zr, Hf, V, Nb, Ta, Cr, Mo and W) are widely used as protective films on cutting tools and other mechanical applications. These films typically in a face-centered cubic (FCC) B1-structure, featuring a closely packed metallic sublattice with nitrogen atoms occupying interstitial positions. This structure brings multi-bonding characteristics of TMNs that could contribute to the cohesive energy, i.e., ionic and metallic, which simultaneously, resulting in exceptional properties such as high hardness, excellent wear resistance and corrosion resistance [1,2]. The properties of TMNs can be finely tuned by varying the concentration of point defects, such as substitutional atoms, interstitial atoms, and vacancies. It is well established that incorporating aluminum (Al) into the B1-type TiN lattice decreases the interatomic distance as the Al content increases, leading to an enhancement in film hardness [3,4]. Additionally, interstitial nitrogen plays a crucial role in the material's mechanical properties. For instance, the addition of 0.52 atomic percent nitrogen has been shown to enhance strength without significantly compromising the ductility of multi-component equiatomic alloys. This is attributed to the interstitial nitrogen atoms, which increase resistance to cross-slip and promote dislocation multiplication [5]. Notably, studies indicate that hardness and elastic modulus of TMNs are highly dependent on the concentration of nitrogen vacancies, processing similar hardening mechanism as those of interstitial nitrogen [6].

Intensive studies have been carried out in recent years to attain improved mechanical performance of multi-principal element nitrides (MPENs) in either conventional or extreme application environments [7–10]. The complex composition feature of MPENs enable further tunable film structure, and thereby allows for structure design with the aim of elevating film mechanical properties. Research on $(HfNbTiVZr)N_x$ films shows that the presence of nitrogen vacancies, i.e., decreasing nitrogen content in substoichiometric nitride, weakening strong and

* Corresponding author. School of Mechanical Engineering, Guizhou University, Guiyang, 550025, PR China.hdu3@gzu.edu.cn

https://doi.org/10.1016/j.jmrt.2024.12.134
Received 12 September 2024; Received in revised form 9 December 2024; Accepted 17 December 2024
Available online 18 December 2024

directional nitrogen p-metal d bonding states, and thereby decreases both film hardness and Young's modulus [11]. Besides, a reduction in lattice constants has been observed as more nitrogen vacant site is incorporated into FCC-type (AlCrMoTaTiZr)N_x lattice, resulting in a decrease in hardness [12]. Similar phenomena are discovered in TiNbZrTa-based nitride system, where the decrease of nitrogen vacant site, i.e., increase of nitrogen anion site, increases film hardness [13,14]. These studies indicate that the mechanical properties of MPENs are generally linearly influenced by the concentration of point defects.

In addition to the anions, the mechanical properties of the above-mentioned MPENs are proved to highly dependent on the nitride-forming ability of the metallic elements. As an example, the strong nitride-forming elements (Hf, Nb, Zr and Ta) contributes the higher hardness of nitrides, while weak nitride-forming elements such as Mo improves film toughness [15]. The strong nitride-forming elements, generally from group IVB and VB, are more chemically stable compared to those in group VIB. It is mainly due to the filling of electrons in antibonding states within the system, e.g., for Mo–N, the cubic B1 structure is energetically unfavorable, whereas a hexagonal structure is preferred. In addition, experimental and theoretical studies prove that the structural evolution of group -VI nitrides is correlated with the number density of nitride vacancies. Studies on Mo–N films indicate that the NaCl-type γ-MoN_x phase is favored with x = 0.30–0.53, while at higher nitrogen contents, e.g., $MoN_{0.67}$, γ′-MoN_x phase with vacant sites on nitrogen sublattice is usually achieved [16]. As such, the combination of strong and weak nitride forming elements in MPENs enables structural tailoring by simply manipulating nitrogen flow rate, and thereby achieving desired film properties in mechanical applications.

In this study, HfMoNbZrTa is selected as the multi-principal element family, where the evolution of structural and mechanical properties within HfMoNbZrTa nitrides with regards to nitrogen content is explored. The deposition process is achieved by using $Hf_{25}Mo_{25}Nb_{25}Zr_{25}$ and Ta co-sputtering by direct current magnetron sputtering. Constant target discharge powers are employed to keep nearly equal-molecular metallic elements in the as-deposited films, with controllable nitrogen percentage by alternating the N_2/Ar flow ratio. The film crystal structure and mechanical properties, accompanied by calculations based on density functional theory (DFT) are then carried out to understand the correlation between film crystallographic structure and mechanical properties. The current study could serve as the basic guidance for composition selection and design for MPENs.

2. Experimental details

2.1. Film deposition

The $(HfMoNbZrTa)_{1-x}N_x$ ($0 \le x \le 0.5$) films were grown in a high vacuum sputtering system using a 3-inch $Hf_{25}Mo_{25}Nb_{25}Zr_{25}$ (99.95% purity) compound target and a Ta (99.8% purity) single-element target in co-sputtering configurations. One-side polished 10 × 10 mm-sized silicon (001) was used as substrates. All substrates were cleaned with petroleum ether and isopropanol for 20 min. Then they were mounted on the substrate holder at a distance of 11 cm from the target surface. Prior to deposition, the targets were sputter etched in Ar (99.997% purity) atmosphere for 5 min to remove contaminants from the target surface by ensuring that the substrate shutter was closed. Films were grown at room temperature, i.e, without external heating. The HfMoNbZrTa alloy interlayer was deposited using direct current magnetron sputtering (dcMS) with a discharge power of 200 W and 50 W for $Hf_{25}Mo_{25}Nb_{25}Zr_{25}$ and Ta targets for 1 min, respectively. $(HfMoNbZrTa)_{1-x}N_x$ films were grown by introducing N_2 (99.997% purity) and Ar (99.997% purity) into the chamber and adjusting the throttle valve to maintain a working pressure of 0.45 Pa. The flow rate of N_2/Ar was set to 0 sccm/40 sccm, 2 sccm/38 sccm, 4 sccm/36 sccm, 6 sccm/34 sccm, 8 sccm/32 sccm, 10 sccm/30 sccm, 12 sccm/28 sccm and 14 sccm/26 sccm, resulting in N_2 flow ratios ($R_N = f_{N_2}/(f_{N_2} + f_{Ar}) \times 100\%$, where f_{N_2} and f_{Ar} are the flow rate of N_2 and Ar, respectively) of 0%, 5%, 10%, 15%, 20%, 25%, 30% and 35%, respectively. Both $Hf_{25}Mo_{25}Nb_{25}Zr_{25}$ and Ta targets were operated in dcMS mode, with target discharge power of 200 W and 50 W respectively, to maintain nearly equal atomic percentages of metallic elements in $(HfMoNbZrTa)_{1-x}N_x$ films. The substrates were kept at floating potential during deposition. All films were deposited for 2 h.

2.2. Film characterization

The crystallographic structures of the films as-deposited were evaluated by X-ray diffraction (XRD) spectrometer (D8 Advance, Bruker) in a Bragg-Brentano (θ-2θ) geometry with the Cu-Kα radiation (λ = 1.540597 Å). The recorded 2θ ranges from 30° to 80° with a step size of 0.01° and a scan speed of 2°/min, with the acceleration voltage and emission current set to 30 kV and 40 mA, respectively. Plan-view and cross-sectional morphologies of the as-deposited films were measured using a scanning electron microscope (SEM, Sigma 300, Zeiss). The elemental composition of the films was evaluated by energy-dispersive spectroscopy (EDS, X-Max, Oxford Instruments) in the same chamber. The film grown at $R_N = 20\%$ was selected for detailed structural analysis by using (scanning) transmission electron microscopy ((S)TEM, Talos F200X G2, ThermoFisher) with a field emission gun operated at 200 kV. The specimen for (S)TEM measurement was prepared with a focused ion beam (FIB, Scios 2 HiVac, ThermoFisher). In this process, a 30 kV Ga ion beam was used for initial polishing, followed by a subsequent 5 kV Ga ion beam for the final polishing stage. Hardness (H) and elastic modulus (E) of the as-deposited films were measured by a nanoindentation tester (TTX-NHT3, Anton Paar) equipped with a Berkovich indenter. The measurement was performed at a load of 5 mN and H and E were obtained from the load-displacement curve according to the method of Oliver and Pharr [17]. 5 indentations were performed for each sample, and H and E values were calculated by averaging the results. H/E and H^3/E^{*2} ratios were calculated to indicate film the elastic deformation response of the films and its resistance to plastic deformation in surface contact [18,19]. The effective elastic modulus (E^*) was estimated using the film elastic modulus (E) and Poisson ratio (ν) [20]. Dry sliding tribological investigations were carried out on a ball-on-disc tribometer (MFT-5000, Rtec) fitted with a 6 mm diameter GCr15 ball in ambient air. The normal load, sliding speed and sliding time were set to 5 N, 200 mm/min and 30 min respectively. The morphologies of the wear tracks were analyzed using a 3D surface profiler (Contour Elite K, Bruker). Wear rates K were calculated using the equation [21]:

$$K = \frac{V}{F \times S}$$

where V is the wear volume (m^3), F is the normal load (N) and S is the sliding distance (m).

2.3. DFT calculation

Calculations based on density functional theory (DFT) were carried out in order to get further understanding of film structure and hardness evolution. A 3 × 3 × 3 HfMoNbZrTa supercell in the BCC ($Im\bar{3}m$) structure and a 2 × 2 × 2 $(HfMoNbZrTa)_{1-x}N_x$ supercell in the FCC ($Fm\bar{3}m$) structure were selected as calculation models. The 3 × 3 × 3 HfMoNbZrTa supercell included 54 metal atoms (Hf: Mo: Nb: Zr: Ta = 11: 11: 11: 11: 10), while the 2 × 2 × 2 $(HfMoNbZrTa)_{1-x}N_x$ supercell consisted of 60 atoms (Hf: Mo: Nb: Zr: Ta: N = 6: 7: 7: 6: 6: 28, $(HfMoNbZrTa)_{32}N_{28}$) and 64 atoms (Hf: Mo: Nb: Zr: Ta: N) = 6: 7: 7: 6: 6: 32, $(HfMoNbZrTa)_{32}N_{32}$), giving a nitrogen percentage of 46.7 at.% and 50 at.%, respectively, in the $(HfMoNbZrTa)_{1-x}N_x$ crystals. All supercells were first constructed via the special quasi-random structures (SQS) method generated using the mcsqs code [22] of the Alloy Theory Automated Toolkit (ATAT) [23]. The density of states (DOS) of

constructed crystals were then calculated by ab-initio calculations based on DFT, using the Vienna Ab Initio Simulation Package (VASP) [24]. The interaction between ions and electrons was simulated using the Projector Augmented Wave (PAW) method [25]. The Generalized Gradient Approximation (GGA) with Perdew-Burke-Ernzerhof (PBE) potential was used to describe the exchange correlation function [26,27]. To ensure that the energy is converged to less than 1 meV per atom, the plane wave cut-off energy was set to 520 eV [28], and the k-mesh over the Brillouin zone was 3 × 3 × 3 Monkhorst-Pack sampling. The energy convergence of self-consistency cycles and ionic relaxation was set up as EDIFFG = −0.001 and EDIFF = 1E-7, respectively. The equilibrium volume was obtained by fitting the third-order Birch-Murnaghan equation of state (EOS) [29]. The calculated results were post-processed by VASPKIT [29]. The theoretical hardness ($H_{theo.}$) of the supercell was calculated using the empirical model of Chen [30]:

$$H_{theo.} = 2\left(G^3/B^2\right)^{0.585} - 3$$

where G and B are the polycrystalline shear and bulk moduli, respectively, of the material under consideration.

3. Results

3.1. Composition and crystal structure

The elemental composition, the atomic ratio between the nitrogen and the total amount of metallic elements (N/Me), and the atomic ratio between Ta and Me (Ta/Me) of $(HfMoNbZrTa)_{1-x}N_x$ films grown at varied R_N are shown in Fig. 1. As can be seen in Fig. 1(a), all metallic elements show nearly equal atomic ratio (±1.9 at.%). With the increase of R_N, the nitrogen content in the as-deposited film increases, while the overall quantity of metallic elements decreases. When $R_N \geq$ 25 %, the N/Me ratio reaches the maximum value of approximately 1 and remains unchanged even with further increases in R_N (Fig. 1(b)). It should be noted that the atomic percentage of Ta shows a variation of approximately 0.02 between the maximum and minimum Ta/Me values, as shown in Fig. 1(c). This discrepancy is unlikely to be caused by differences in the hysteresis behavior of the Ta and $Hf_{25}Mo_{25}Nb_{25}Zr_{25}$ targets due to the absence of a linear trend in the Ta/Me ratio.

Fig. 2 shows X-ray diffractograms of the $(HfMoNbZrTa)_{1-x}N_x$ films, including calculated X-ray diffractogram for HfMoNbZrTa, $(HfMoNbZrTa)_{32}N_{28}$ and $(HfMoNbZrTa)_{32}N_{32}$ (corresponding to R_N = 0%, 20%, and 35%, respectively), and the corresponding theoretical and experimental position of the peak in between 2θ = 34° and 38° for HfMoNbZrTa, $(HfMoNbZrTa)_{32}N_{28}$ and $(HfMoNbZrTa)_{32}N_{32}$. In Fig. 2 (a), the films grown under inadequate nitrogen flow rate ($R_N \leq$ 5%) show low crystallinity with body-centered cubic (BCC) 110 reflections, consistent with previous findings where the HfMoNbZr-based alloy films predominantly form an amorphous matrix under RT or 500 °C [31,32]. It is also clear that the BCC 110 diffraction peak shifts to lower 2θ angles as nitrogen is incorporated into the film. As R_N increases to 10%, higher crystallinity FCC NaCl-type crystallographic structures with 111, 200, 220, 311 and 222 predominant diffraction peaks are seen at 2θ = 35.2°, 40.8°, 59.0°, 70.5° and 74.3°, respectively. However, diffraction peaks corresponding to the hexagonal structured η-TaN (004) and γ-Ta_2N (100) planes (ICSD-644728, $P6_3/mmc$, space group 194 and ICSD-290431, $P6_3/mmc$, space group 194, respectively) and β-Mo_2N (112) peak (ICSD-30593, $I4_1/amd$, space group 141) are seen when R_N = 20%. At 10% ≤ R_N ≤ 20%, the 111 peak intensity increases while that of the 200 peak intensity decreases with the increase of R_N. On the contrary, for the $R_N \geq$ 25% cases, the peak intensity of 200 increases with increasing R_N, accompanied by a simultaneous decrease of 111 peak intensity. For all the films grown at $R_N \geq$ 10%, the reflections from the FCC planes shift to lower diffraction angles with the increase of R_N, indicating an increase of the out-of-plane lattice constant (a_0) due to the increasing amount of nitrogen incorporation in the crystallites (see examples of a_0 calculated using 111 and 200 peak in Fig. S1). This trend is supported by the theoretical shift shown in Fig. 2(b)–(c), where the theoretical peak position shifts to lower angles when comparing HfMoNbZrTa (R_N = 0%), $(HfMoNbZrTa)_{32}N_{28}$ (R_N = 20%) and $(HfMoNbZrTa)_{32}N_{32}$ (R_N = 35%) cases. It is noteworthy that all experimental reflections show lower peak positions as compared with those of theoretical, which is mainly due to the increased lattice distortion under the ion irradiation of rare gas ions [32].

The cross-sectional morphologies of $(HfMoNbZrTa)_{1-x}N_x$ films are illustrated in Fig. 3. The as-deposited films (R_N = 0% and 5%) show a glass-like feature in the cross section which is consistent with the identified broadened X-ray diffraction peaks (Fig. 2). As R_N increases, the nitrogen containing films tend to grow towards columnar structure, while with $R_N \geq$ 30% the columnar structure is slightly weakened. This phenomenon is in agreement with the previous studies [33–35] which suggested the high nitrogen flow rate leads to a disordered film growth.

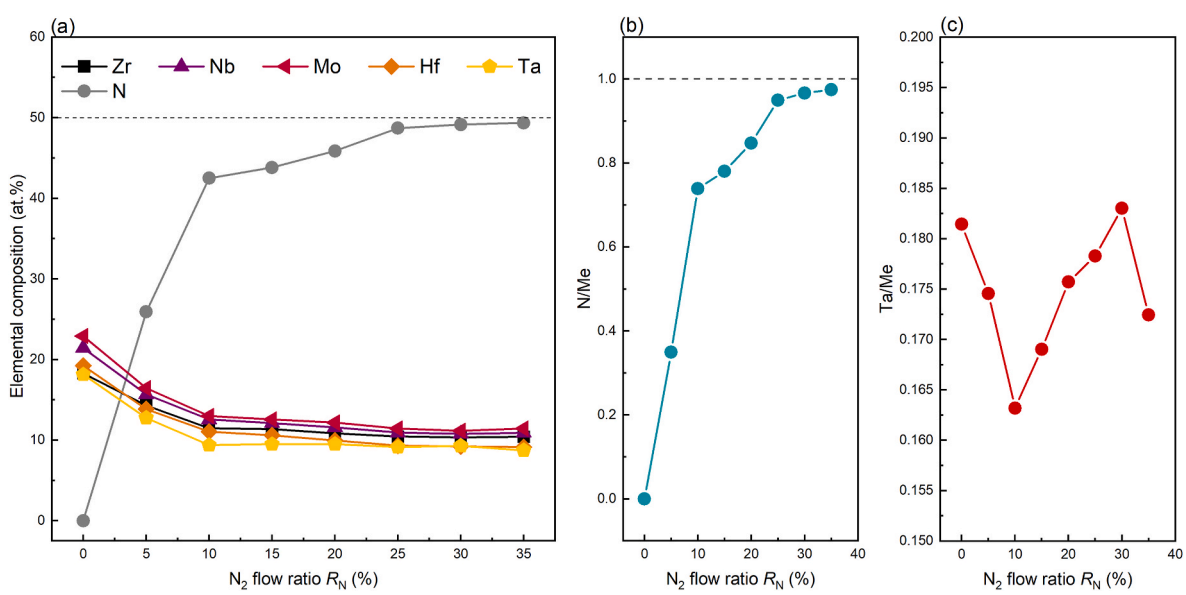

Fig. 1. (a) Elemental composition, (b) the atomic ratio between the nitrogen and the total amount of metallic elements (N/Me), and (c) the atomic ratio between Ta and Me (Ta/Me) of $(HfMoNbZrTa)_{1-x}N_x$ films grown at N_2 flow ratio (R_N) ranges from 0% to 35%.

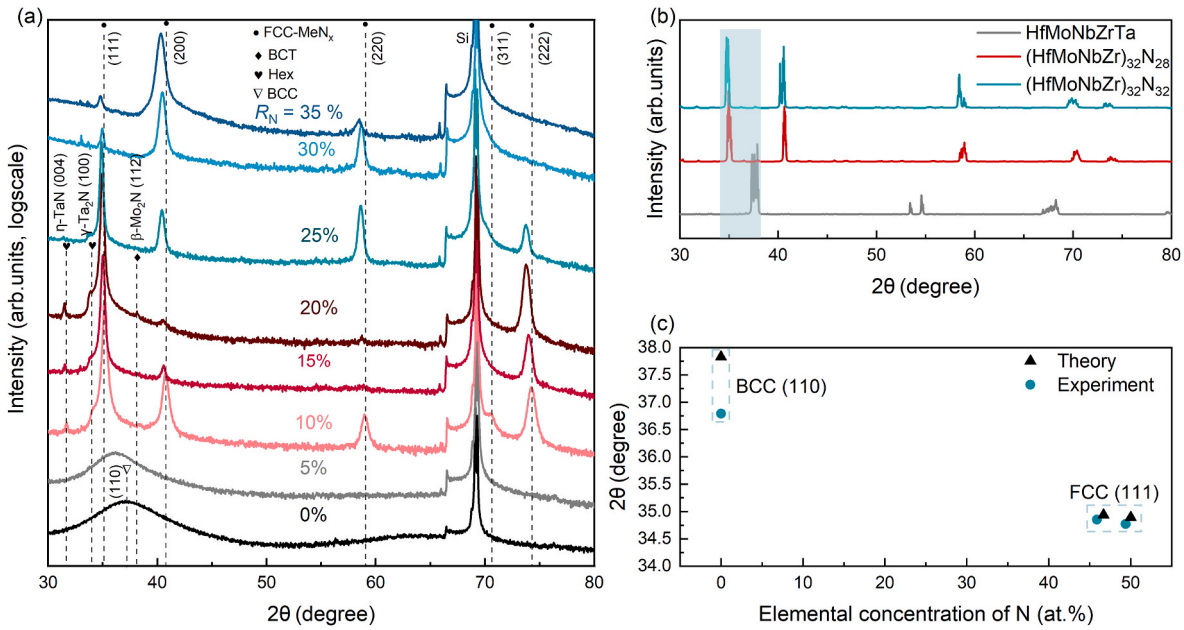

Fig. 2. (a) X-ray diffractograms of $(HfMoNbZrTa)_{1-x}N_x$ films grown at N_2 flow ratio (R_N) ranging from 0% to 35%. (b) The calculated X-ray diffractogram and (c) theoretical and experimental position of the peak in between 2θ = 34° and 38° of HfMoNbZrTa, $(HfMoNbZrTa)_{32}N_{28}$ and $(HfMoNbZrTa)_{32}N_{32}$ supercell (corresponding to R_N = 0%, 20%, and 35%, respectively). Theoretical X-ray diffractograms in between 2θ = 34° and 38° shown in (b) are framed in blue box. Theoretical and experimental diffraction positions from BCC (110) and FCC (111) planes in between 2θ = 34° and 38° shown in (c) are framed by blue dashed lines.

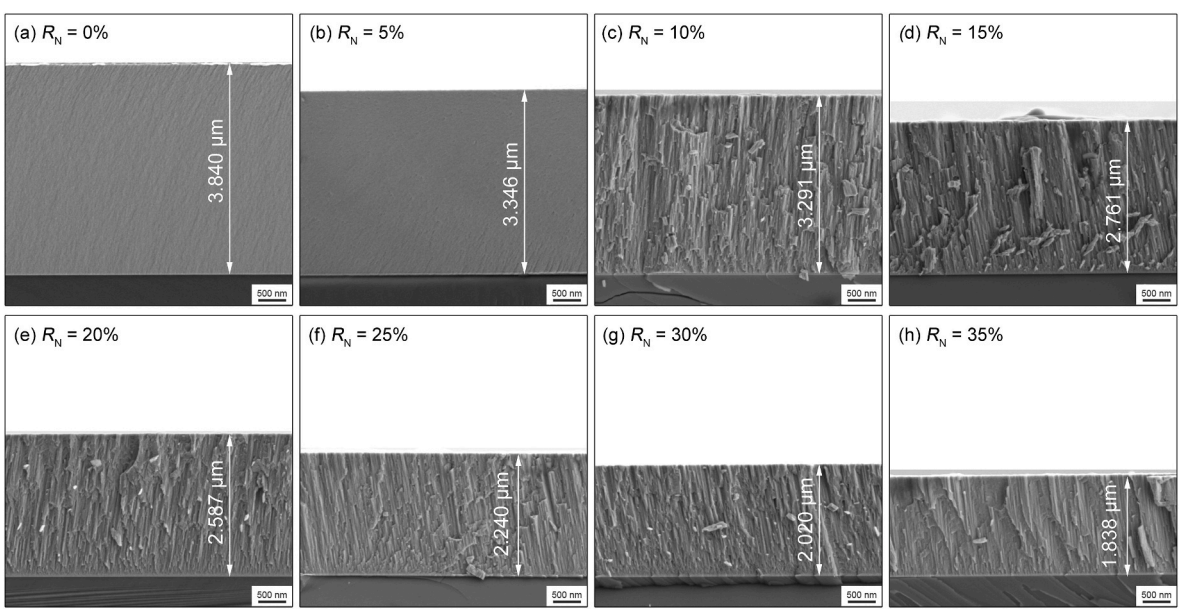

Fig. 3. Cross-sectional SEM micrographs of $(HfMoNbZrTa)_{1-x}N_x$ films deposited at N_2 flow ratio (R_N) of (a) 0, (b) 5%, (c) 10%, (d) 15% (e) 20% (f) 25%, (g) 30% and (h) 35%. The measured thickness of as-deposited films is labelled.

In addition, with the increase of R_N, the growth rate of these films decreases, correlating with the lower sputtering yield of nitrides formed on the metallic target at high R_N.

To get a better understanding of the crystallographic structure and the elemental distribution of the grown film, cross-sectional TEM and EDS mapping are performed for the $(HfMoNbZrTa)_{1-x}N_x$ film grown at R_N = 20% (Fig. 4). As shown in Fig. 4(a), the EDS mapping of the film indicates uniform distributions of Hf, Mo, Nb, Zr, Ta, and N throughout the film, with no noticeable elemental segregation. The low-resolution cross-sectional image in Fig. 4(b) reveals the typical columnar structure of the as-deposited film, consistent with the observations in Fig. 3, which should compare with the nearly amorphous structure of the HfMoNbZrTa film (Fig. S2). Stacking faults (SFs) are also observed in the vicinity of grain boundaries as indicated in Fig. 4(b). In Fig. 4(f)–(h), crystallites in FCC and hexagonal structures, and FCC-structured SFs are identified as evidenced by their Fast Fourier Transformation (FFT) patterns (see Fig. 4(i)–(k)).

3.2. Mechanical property

The values of H, E, H/E, and H^3/E^{*2} for $(HfMoNbZrTa)_{1-x}N_x$ films are shown in Fig. 5. As is depicted in Fig. 5(a), for 5% ≤ R_N ≤ 20%, which corresponds to sub-stoichiometric film regime, the H and E of the as-deposited films are significantly improved with the increasing R_N.

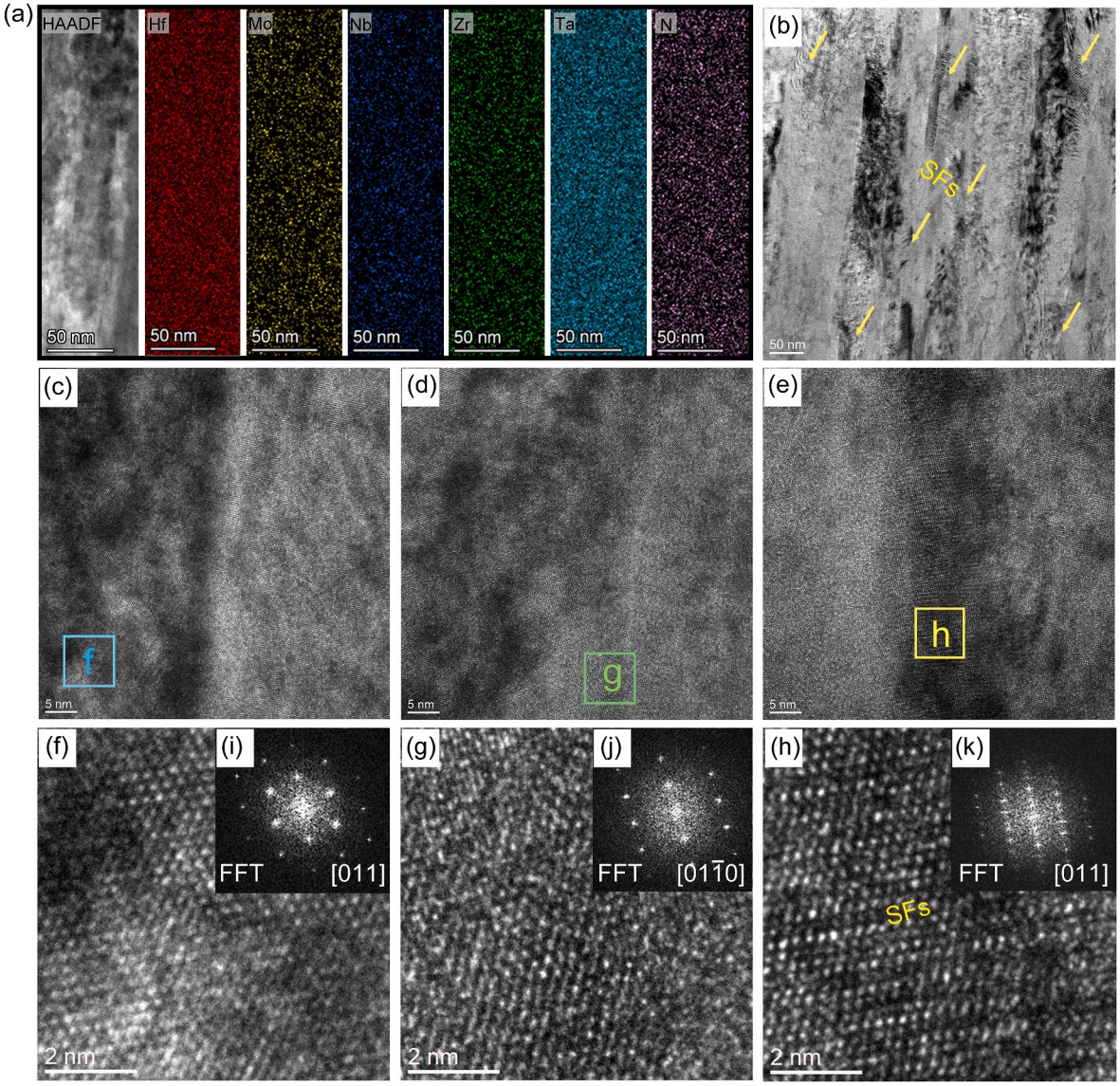

Fig. 4. Cross-sectional (S)TEM images and EDS mapping of the $(HfMoNbZrTa)_{1-x}N_x$ films grown at $R_N = 20\%$. (a) EDS mapping of Hf, Mo, Nb, Zr, Ta, and N. (b) Low-resolution and (c)–(e) high-resolution cross-sectional images of the film at varied positions. (f)–(h) high-resolution images selected from blue-boxed, green-boxed, and yellow-boxed area in (c)–(e), respectively. (i)–(k) are the Fast Fourier Transformation (FFT) patterns of (f)–(h).

However, this trend reverses when R_N reaches 20%, as H gradually decreases with further increases in R_N. A similar trend is observed in the changes of the H/E and H^3/E^{*2} ratios as R_N increases, where maximum values occurring at $R_N = 20\%$ (Fig. 5(b)). Notably, a similar H/E value is achieved for $20\% \leq R_N \leq 30\%$. Since higher H/E and H^3/E^{*2} values generally indicate better abrasion resistance of the films, it can be inferred that the optimal abrasion resistance is achieved when the N_2 flow ratio ranges between 20% and 30% [18].

3.3. Tribological property

The coefficient of friction (COF) as a function of sliding time, wear track 2D profiles, average COF, and wear rate of the $(HfMoNbZrTa)_{1-x}N_x$ films grown at varied R_N are shown in Fig. 6. As shown in Fig. 6(a), all films exhibit typical tribological stages: the COF rises sharply in the run-in period due to the high surface roughness of the film and counterpart, followed by gradual smoothing of the interface leading to a near-stable COF value during the steady-state period [36]. A much lower COF value (~0.4), accompanied by significant fluctuation of COF curve at steady-state period is seen for the $R_N = 0\%$ film as compared with films grown at higher R_N. This indicates a complete failure of the film (see the wear depth in Fig. 6(c)), which is in line with the reported phenomenon [8,31]. As R_N increases to 5%, the COF value is still low but with a much lower wear depth as compared with that of $R_N = 0\%$ film, i.e., without any film wear-out phenomenon. Higher COF values are seen for film grown at R_N ranges from 10% to 35%, which is identical to the previous article [37]. However, slightly lower average COF values are observed for $R_N = 15\%$, 20%, and 35% are identified as compared with those in the same R_N range (Fig. 6(b)). As shown in Fig. 6(c) and (d), the wear depth of wear track for $R_N = 35\%$ film is much higher than the films grown at $5\% \leq R_N \leq 30\%$ which is identical with the estimated wear rate of films in Fig. 6(e) that the $R_N = 35\%$ film exhibits the highest wear rate. As seen in Fig. 6(d) and (e), $R_N = 25\%$ film generally has the lowest wear track depth and wear rate.

3.4. Density of states and electron localization function

To further understand the structural evolution of the films at varied nitrogen content, calculations based on DFT are performed. Total density of states (TDOSs) of HfMoNbZrTa, $(HfMoNbZrTa)_{32}N_{28}$ and

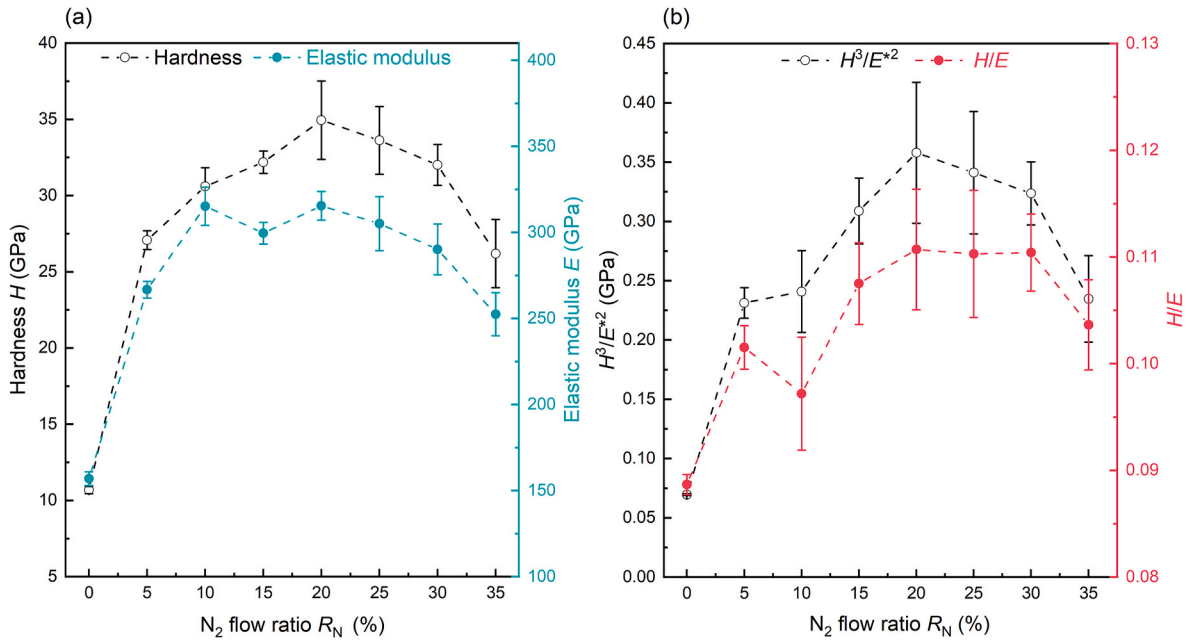

Fig. 5. (a) Hardness (H) and elastic modulus (E), and (b) H/E and H^3/E^{*2} of $(HfMoNbZrTa)_{1-x}N_x$ films on Si substrates deposited at different N_2 flow ratio (R_N).

$(HfMoNbZrTa)_{32}N_{32}$ (corresponding to R_N = 0%, 20%, and 35%, respectively), and the partial electronic density of states (PDOSs) of $(HfMoNbZrTa)_{32}N_{32}$ are shown in Fig. 7. As seen in Fig. 7(a), the TDOSs values of the crystals are all not zero at E_F, showing metallic characteristics for both HfMoNbZrTa alloy and nitrides. However, the TDOSs value at E_F decreases with the increasing N, indicating an increase of chemical stability of crystals. In addition, $(HfMoNbZrTa)_{32}N_{32}$ shows the closest position of pseudo gap (P_{gap}) to E_F (marked with a black dashed circle in Fig. 7(a)). As the shift of P_{gap} position in the TDOSs correlates with changes in Me–N bond strength, $(HfMoNbZrTa)_{32}N_{32}$ thereby exhibits highest bond strength [38]. As illustrated by PDOSs of the elements in $(HfMoNbZrTa)_{32}N_{32}$ (see Fig. 7(b)), the d-orbitals of metallic elements and p-orbitals of N have hybrid phenomena at the energy of −9 to −3 eV demonstrating that Me–N bonds exists between the metallic atom and the nitrogen [39].

To further elucidate the bonding structure, electron localization function (ELF) of HfMoNbZrTa, $(HfMoNbZrTa)_{32}N_{28}$ and $(HfMoNbZrTa)_{32}N_{32}$ are calculated. (100) plane ELF of the crystals are shown in Fig. 8. For HfMoNbZrTa, metallic atoms are surrounded by lower ELF values, which is in line with DOS results (Fig. 7). This structure is interrupted by the incorporation of N into the system as higher ELF is formed around the N atoms, indicating a higher degree of localization of the Me–N bond [9].

4. Discussion

An evolution of film crystallographic structure regarding the varied R_N is generally identified in Figs. 1–4. The observed structure of $(HfMoNbZrTa)_{1-x}N_x$ films with low N concentration (typically the case $R_N = 5\%$) is nearly amorphous which is similar with that of HfMoNbZrTa film ($R_N = 0\%$, see Fig. S2) but with nitrogen defects, resulting in a shift of reflections to lower 2θ angles. The shift of diffraction peak follows the DFT calculations where the incorporation of N causes an expansion of lattice (see Fig. 2(b) and (c)). As $10\% \leq R_N \leq 20\%$, multi-phase structure, containing η-TaN and γ-Ta_2N, is achieved, followed by β-Mo_2N appearing at $R_N = 20\%$. The formation of multi-phase is mainly due to the insufficient nitrogen in the film [40]. In particular, it has been reported that β-MoN_x preferentially forms at low nitrogen partial pressure as well as low growth temperature which transforms to FCC-structured γ-Mo_2N at high nitrogen partial pressure [41–44]. Moreover, according to Ref. [45], the enthalpies of mixing of N with Hf, Nb, Zr, Ta, and Mo were identified as −218, −174, −233, −173, and −115 kJ/mol, respectively, indicating that Mo–N is not as stable as the other nitrides [8]. Despite the similar mixing enthalpies of N with Ta and Nb, Ta–N phases exhibit lower stability compared to Nb–N phases within the same group, as reflected in the higher equilibrium pressure required for their formation [46].

The X-ray diffractograms (Fig. 2(a)) clearly show a shift in the preferred orientation of the FCC phase, transitioning from the (111) plane to the (200) plane, with the increase of R_N. The mechanism of texture evolution for transition-metal nitrides are actually similar: the (111) plane possesses the lower strain energy and higher surface energy as compared to that of the (100) plane, of which the texture transforms toward 111 when strain energy between (111) plane and (100) plane is enlarged as compared with the surface energy between these two planes [47]. In this study, films grown at $R_N \leq 25\%$ are non-stoichiometric, i.e., with high number density of nitrogen vacancy defects, resulting in the deviation of lattice parameter from ideal one. The lattice strain generated by nitrogen vacancy will thus induce a film growth dominated by (111) plane. This lattice strain will be released as more nitrogen is introduced into the lattice, which results in a texture transformation from 111 to 200. It should be noted that the texture evolution can also be attributed by the incident particle energy. Greene et al. [48] suggested that the higher incident energy leads to larger adatom mobility, inducing a change in film growth direction from [111] to [100], i.e., from the (111) plane to the (200) plane. In this study, the evolution of film growth orientation is not expected to be related to the incident particle energy, as the substrate was kept floating and there was no significant change in the discharge voltage for all series.

The hardness of $(HfMoNbZrTa)_{1-x}N_x$ film increases and then decrease with the increasing of R_N (Fig. 5), where only the $R_N = 35\%$ reaches N/Me value of ~1 (Fig. 1). In our results, the increasing hardness of as-deposited film at elevated R_N indicates high correlation with the change in TDOSs and ELF values (Figs. 7 and 8), where higher localized Me–N bond is formed resulting in higher local lattice distortion [32]. However, this mechanism is not able to explain the hardness decrease with further increase of R_N ($R_N > 20\%$) as the higher bond strength formed in Me–N will not cause any hardness deterioration with the further nitrogen incorporation in the substoichiometric nitride. Indeed, some research reported a significant hardness increase when dual-phase

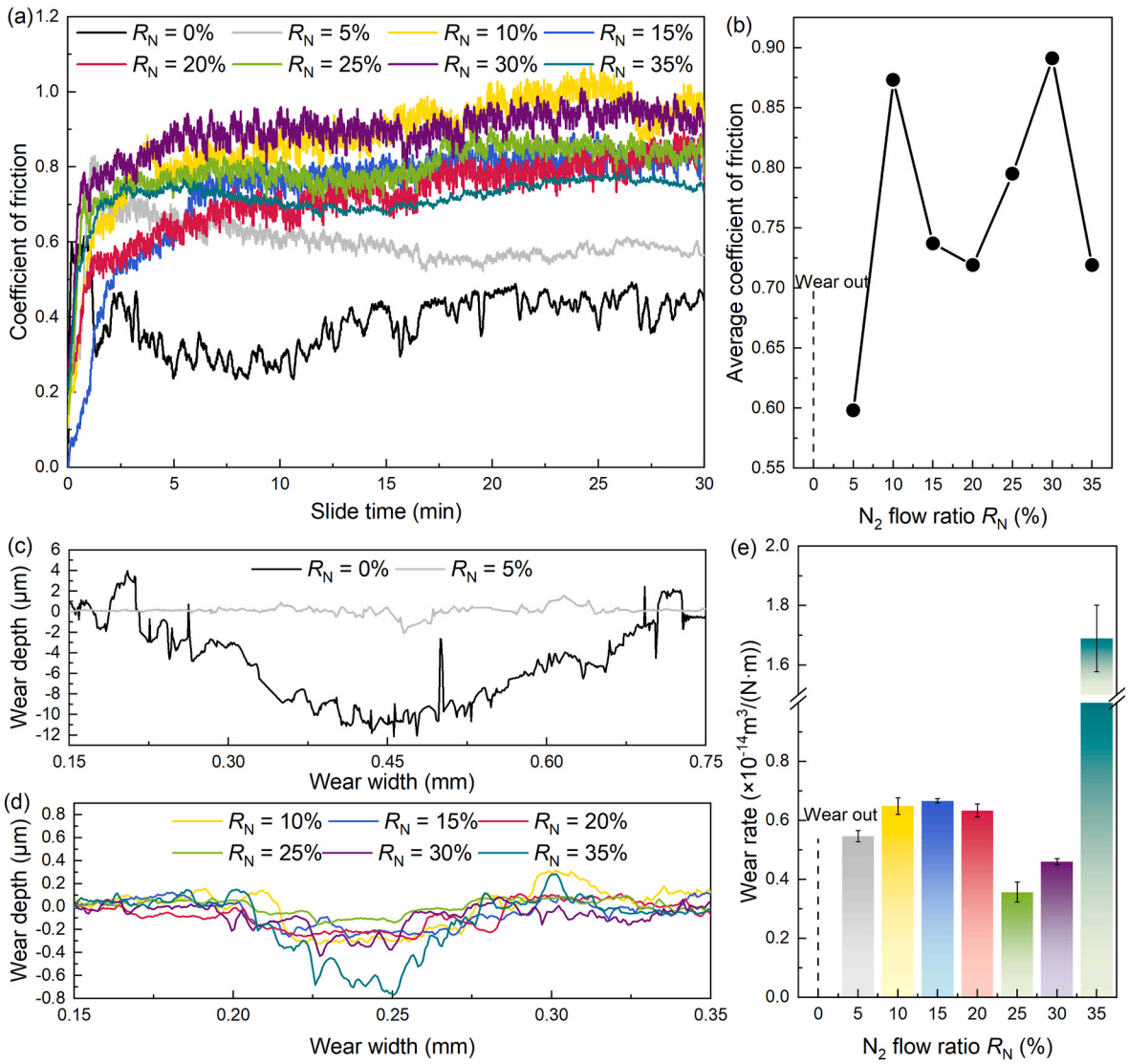

Fig. 6. (a) Coefficient of friction (COF) as a function of sliding time, (b) average COF, (c) and (d) 2D profiles of wear tracks, and (e) wear rate of the $(HfMoNbZrTa)_{1-x}N_x$ films deposited at different N_2 flow ratio (R_N). The wear rate in (e) is averaged from 3 measurements.

structure is formed in the film, attributed to distinct plastic deformation mechanisms and interface interactions within the structure [31,49–51]. Here, the observed multi-phase structure of the as-deposited film at 10% $\leq R_N \leq$ 20% also contributes to increased film hardness (see Fig. 4(f)–(g)). Moreover, as SFs are observed in the vicinity of grains for $(HfMoNbZrTa)_{1-x}N_x$ film grown at $R_N = 20\%$ (see Fig. 4(b)–(e), and (h)), we also attribute the increase in hardness to interface hardening resulted from the introduction of planar defects. The high density SFs serve as barriers to dislocation motion, thus further increase the hardness [52, 53]. As the multi-phase structure disappears at higher R_N, film hardness gradually decreases. In addition, the texture changes from 111 to 200 is also supposed to cause a film hardness drop as shown elsewhere [54]. To further support the above conclusion, we calculate the theoretical hardness of single-phase $(HfMoNbZrTa)_{1-x}N_x$ supercell with nitrogen concentration of 0, 46.7, and 50 at.%, respectively (with the same model in Figs. 7–8), and compared with trends observed in films grown at varied R_N (Fig. 5). The theoretical hardness increases with the increase of nitrogen percentage, which is consistent with our previous conclusion that the Me–N bond strength gradually becomes stronger with the increase of N content, leading to higher hardness. However, this trend is different from the experimental one as higher hardness is achieved by the film with nitrogen concentration of 46.7 at.% instead of the 50 at.% series. It should be noted that the calculation of $H_{theo.}$ considers only the changes in shear modulus and the bulk modulus following the nitrogen concentration in the crystal, and thus the absolute value is not comparable between $H_{theo.}$ and H [30]. In general, the strengthening mechanism mentioned above is further proved by the results shown in Fig. 9. The strengthening of film by means of multi-phase structure is also shown to benefit film tribology performance where films grown at 20% $\leq R_N \leq$ 30% exhibits lowest wear rate. As higher H/E and H^3/E^{*2} represent higher elastic strain to failure and enhanced resistance of the film to plastic deformation, we attribute the elevated tribological performance of films grown at this R_N range to the higher H/E and H^3/E^{*2} values (see Fig. 5). In general, we demonstrate the positive effect of multi-phase structure on the mechanical properties of grown $(HfMoNbZrTa)_{1-x}N_x$ films, where the structure can be simply tuned by varying the nitrogen concentration within the film. Based on the present work, we expect great interest in quantifying the effect of multi-phase on the film properties as well as tailoring such structures using other methods, e.g., ion bombardment from energetic particles.

5. Conclusion

In this study, we demonstrate the structure and properties of

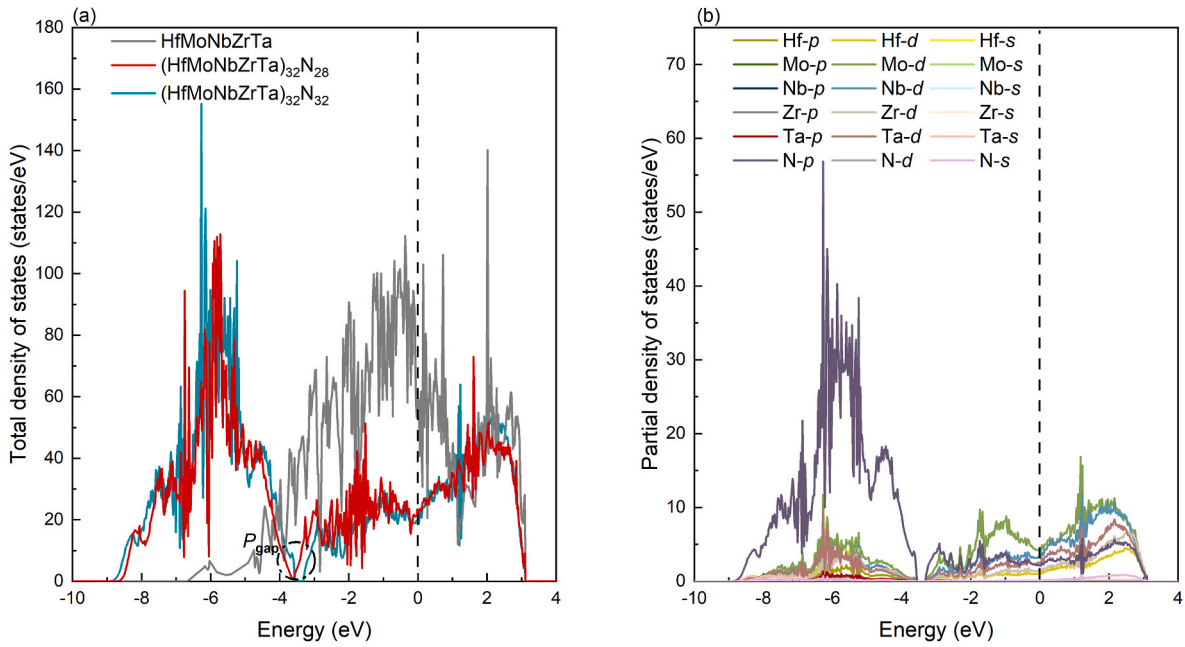

Fig. 7. (a) The total density of states (TDOSs) of HfMoNbZrTa, $(HfMoNbZrTa)_{32}N_{28}$ and $(HfMoNbZrTa)_{32}N_{32}$, where pseudo gaps (P_{gap}) are marked with a black dashed circle. (b) The partial density of states (PDOSs) of $(HfMoNbZrTa)_{32}N_{32}$. The Fermi level is set to 0 eV marked by a vertical dashed line.

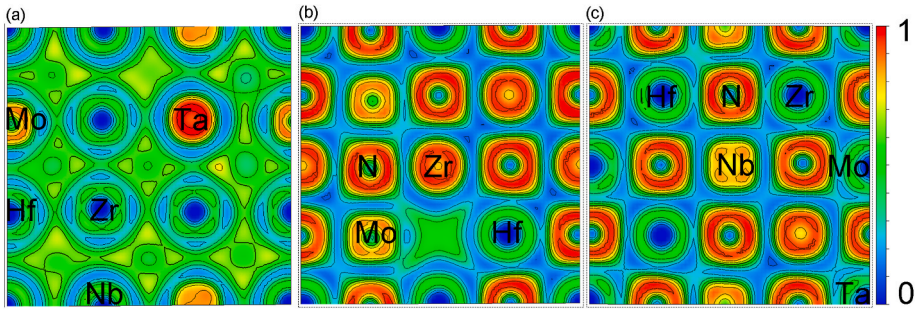

Fig. 8. The electron localization function (ELF) of (a) HfMoNbZrTa, (b) $(HfMoNbZrTa)_{32}N_{28}$, (c) $(HfMoNbZrTa)_{32}N_{32}$ in (100) plane. ELF = 0 and ELF = 1 correspond to the delocalized state and the localized states, respectively. The ELF = 0.5 corresponds to a uniform electron gas.

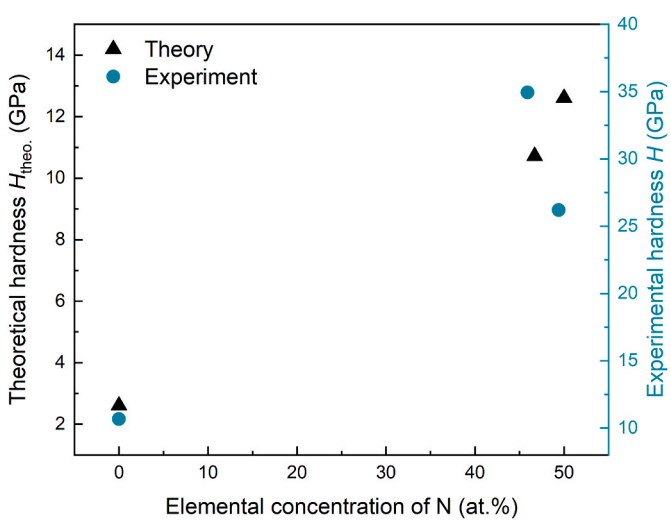

Fig. 9. Theoretical hardness ($H_{theo.}$) and experimental hardness (H) of $(HfMoNbZrTa)_{1-x}N_x$ at the similar elemental concentration of nitrogen.

$(HfMoNbZrTa)_{1-x}N_x$ films are highly dependent on the nitrogen content, which can be used for tailoring film properties for varied applications. At $R_N \leq 5\%$, the crystallographic structure of the as-deposited film is mainly composed of nearly amorphous body-centered cubic (BCC) structure, with the peak position shifting to low diffraction angles as R_N increases. A face-centered cubic (FCC) predominated multi-phase structure appears at $10\% \leq R_N \leq 20\%$ with a strong (111) crystallographic orientation of the FCC phase. When $R_N \geq 25\%$, the multi-phase structure transitions to a single-phase FCC-type structure, accompanied by a preferred orientation change from (111) to (200) with increasing R_N. The highest hardness, peaking at 34.9 ± 2.6 GPa, is achieved for $R_N = 20\%$, where a multi-phase structured substoichiometric film is identified. The trend of hardness measured from the as-deposited film in relation to nitrogen content significantly differs from that of single-phase material calculated based on density functional theory (DFT), indicating that the high hardness is partly attributed to the formation of multi-phase structures. The overall change in wear rate approximately correlates with hardness, with the minimal wear rate of 3.6×10^{-15} $m^3/(N \cdot m)$ achieved by the film grown at $R_N = 25\%$. This research, in general, furnishes new insights into the effect of nitrogen content on the crystallographic structure of $(HfMoNbZrTa)_{1-x}N_x$ films, revealing new possibilities for tailoring the mechanical properties of MPENs through structural design.

CRediT authorship contribution statement

Yiming Ruan: Conceptualization, Investigation, Methodology, Data curation, Formal analysis, Writing – original draft. **Jigang Xie:** Data curation, Writing – review & editing. **Lin He:** Project administration, Conceptualization, Supervision, Writing – review & editing. **Fugui Zhang:** Writing – review & editing, Funding acquisition. **Jie Shi:** Investigation, Data curation, Formal analysis, Writing – review & editing. **Hengning Hu:** Investigation, Writing – review & editing. **Yun Chen:** Investigation, Writing – review & editing. **Rui Shu:** Conceptualization, Investigation, Methodology, Funding acquisition, Writing – review & editing. **Liuquan Yang:** Conceptualization, Investigation, Methodology, Funding acquisition, Writing – review & editing. **Hao Du:** Project administration, Conceptualization, Methodology, Supervision, Writing – review & editing, Funding acquisition.

Data availability

The data that support these findings are available from the corresponding author on request.

Declaration of competing interest

The authors declare that they have no known competing financial interests or personal relationships that could have appeared to influence the work reported in this paper.

Acknowledgments

The work is financially supported by the National Natural Science Foundation of China (Grant No. 52165021 and 51805102), SINOMACH (Grant No. JG04KF0202301), Guizhou Provincial Science and Technology Innovation Centre (Grant No. [2023]010), and the Guizhou University Cultivation Project (Grant No. [2019] 25). Rui Shu acknowledges support from the Swedish Research Council VR International Postdoc Grant 2022-00213. Liuquan Yang acknowledges the financial support by the Engineering and Physical Sciences Research Council (EPSRC, Grant No. EP/X52573X/1) in the UK. Hao Du is grateful for the backing of SuPro Instruments Co., Ltd, Ionautics AB, and the State Key Laboratory of Public Big Data at Guizhou University. Dr. Jianjun Hu at University of South Carolina is appreciated for the help and support for DFT calculations.

Appendix A. Supplementary data

Supplementary data to this article can be found online at https://doi.org/10.1016/j.jmrt.2024.12.134.

References

[1] Kindlund H, Sangiovanni DG, Petrov I, Greene JE, Hultman L. A review of the intrinsic ductility and toughness of hard transition-metal nitride alloy thin films. Thin Solid Films 2019;688:137479. https://doi.org/10.1016/j.tsf.2019.137479.
[2] Hu C, Guo K, Li Y, Gu Z, Quan J, Zhang S, Zheng W. Optical coatings of durability based on transition metal nitrides. Thin Solid Films 2019;688:137339. https://doi.org/10.1016/j.tsf.2019.05.058.
[3] Tentardini EK, Aguzzoli C, Castro M, Kunrath AO, Moore JJ, Kwietniewski C, Baumvol IJR. Reactivity between aluminum and (Ti,Al)N coatings for casting dies. Thin Solid Films 2008;516:3062–9. https://doi.org/10.1016/j.tsf.2007.10.088.
[4] Zhou M, Makino Y, Nose M, Nogi K. Phase transition and properties of Ti-Al-N thin films prepared by r.f.-plasma assisted magnetron sputtering. Thin Solid Films 1999; 339:203–8. https://doi.org/10.1016/S0040-6090(98)01364-9.
[5] Li H. Enhanced strength-ductility synergy via high dislocation density-induced strain hardening in nitrogen interstitial CrMnFeCoNi high-entropy alloy. J Mater Sci 2023;141:184–92. https://doi.org/10.1016/j.jmst.2022.09.020.
[6] Shin C-S, Gall D, Hellgren N, Patscheider J, Petrov I, Greene JE. Vacancy hardening in single-crystal TiNx (001) layers. J Appl Phys 2003;93:6025–8. https://doi.org/10.1063/1.1568521.
[7] Chen L, Li W, Liu P, Zhang K, Ma F, Chen X, Zhou H, Liu X. Microstructure and mechanical properties of (AlCrTiZrV)Nx high-entropy alloy nitride films by reactive magnetron sputtering. Vacuum 2020;181:109706. https://doi.org/10.1016/j.vacuum.2020.109706.
[8] Liu W, Wang CT, Zhao SC, Chen L, Li YT, Jiang X, Leng YX. Enhancing wear resistance: in-situ ceramic phase precipitation for strengthening and toughening FeCoNiCrNx high-entropy alloy films. Surf Coat Technol 2024;478:130466. https://doi.org/10.1016/j.surfcoat.2024.130466.
[9] Zhao Y, Jiang M, Xu J, Xie Z-H, Munroe P. Effects of nitrogen concentration on the microstructure and mechanical properties of nanocrystalline (TiZrNbTaMo)N high-entropy nitride coatings: experimental investigations and first-principles calculations. Vacuum 2024;219:112715. https://doi.org/10.1016/j.vacuum.2023.112715.
[10] Shu R, Du H, Sadowski G, Dorri MM, Rosen J, Sortica MA, Primetzhofer D, Lundin D, Le Febvrier A, Eklund P. Multicomponent TixNbCrAl nitride films deposited by dc and high-power impulse magnetron sputtering. Surf Coat Technol 2021;426:127743. https://doi.org/10.1016/j.surfcoat.2021.127743.
[11] Hsu S-Y, Lai Y-T, Chang S-Y, Tsai S-Y, Duh J-G. Combinatorial synthesis of reactively co-sputtered high entropy nitride (HfNbTiVZr)N coatings: microstructure and mechanical properties. Surf Coat Technol 2022;442:128564. https://doi.org/10.1016/j.surfcoat.2022.128564.
[12] Cheng K-H, Lai C-H, Lin S-J, Yeh J-W. Structural and mechanical properties of multi-element (AlCrMoTaTiZr)Nx coatings by reactive magnetron sputtering. Thin Solid Films 2011;519:3185–90. https://doi.org/10.1016/j.tsf.2010.11.034.
[13] Shu R, Lundin D, Xin B, Sortica MA, Primetzhofer D, Magnuson M, Le Febvrier A, Eklund P. Influence of metal substitution and ion energy on microstructure evolution of high-entropy nitride (TiZrTaMe)N1−x (me = Hf, Nb, Mo, or Cr) films. ACS Appl Electron Mater 2021;3:2748–56. https://doi.org/10.1021/acsaelm.1c00311.
[14] Shu R, Paschalidou E-M, Rao SG, Bakhit B, Boyd R, Moro MV, Primetzhofer D, Greczynski G, Nyholm L, Le Febvrier A, Eklund P. Effect of nitrogen content on microstructure and corrosion resistance of sputter-deposited multicomponent (TiNbZrTa)Nx films. Surf Coat Technol 2020;404:126485. https://doi.org/10.1016/j.surfcoat.2020.126485.
[15] Li J, Chen Y, Zhao Y, Shi X, Wang S, Zhang S. Super-hard (MoSiTiVZr)Nx high-entropy nitride coatings. J Alloys Compd 2022;926:166807. https://doi.org/10.1016/j.jallcom.2022.166807.
[16] Klimashin FF, Koutná N, Euchner H, Holec D, Mayrhofer PH. The impact of nitrogen content and vacancies on structure and mechanical properties of Mo–N thin films. J Appl Phys 2016;120:185301. https://doi.org/10.1063/1.4966664.
[17] Oliver WC, Pharr GM. An improved technique for determining hardness and elastic modulus using load and displacement sensing indentation experiments. J Mater Res 1992;7:1564–83. https://doi.org/10.1557/JMR.1992.1564.
[18] Du H, Wang L, Young M, Zhao H, Xiong J, Wan W. Structure and properties of lanthanum doped AlCrN coatings. Surf Coat Technol 2018;337:439–46. https://doi.org/10.1016/j.surfcoat.2018.01.060.
[19] Leyland A, Matthews A. On the significance of the H/E ratio in wear control: a nanocomposite coating approach to optimised tribological behaviour. Wear 2000; 246:1–11. https://doi.org/10.1016/S0043-1648(00)00488-9.
[20] Musil J, Kunc F, Zeman H, Polakova H. Relationships between hardness, Young's modulus and elastic recovery in hard nanocomposite coatings. Surf Coat Technol 2002;154:304–13. https://doi.org/10.1016/S0257-8972(01)01714-5.
[21] Archard JF. Contact and rubbing of flat surfaces. J Appl Phys 1953;24:981–8. https://doi.org/10.1063/1.1721448.
[22] Van De Walle A, Tiwary P, De Jong M, Olmsted DL, Asta M, Dick A, Shin D, Wang Y, Chen L-Q, Liu Z-K. Efficient stochastic generation of special quasirandom structures. Calphad 2013;42:13–8. https://doi.org/10.1016/j.calphad.2013.06.006.
[23] Van De Walle A. Multicomponent multisublattice alloys, nonconfigurational entropy and other additions to the Alloy Theoretic Automated Toolkit. Calphad 2009;33:266–78. https://doi.org/10.1016/j.calphad.2008.12.005.
[24] Kohn W, Sham LJ. Self-consistent equations including exchange and correlation effects. Phys Rev 1965;140:A1133–8. https://doi.org/10.1103/PhysRev.140.A1133.
[25] Blöchl PE. Projector augmented-wave method. Phys Rev B 1994;50:17953–79. https://doi.org/10.1103/PhysRevB.50.17953.
[26] Perdew JP, Wang Y. Accurate and simple analytic representation of the electron-gas correlation energy. Phys Rev B 1992;45:13244–9. https://doi.org/10.1103/PhysRevB.45.13244.
[27] Perdew JP, Burke K, Ernzerhof M. Generalized gradient approximation made simple. Phys Rev Lett 1996;77:3865–8. https://doi.org/10.1103/PhysRevLett.77.3865.
[28] Liu H, Du H, Xian G, Chen Y, Dai H. Ab-initio calculations of corundum structured α-(Al0.75Cr0.22Me0.03)2O3 compounds (Me = Si, Fe, Mn, Ti, V and Y). Comput Mater Sci 2022;212:111601. https://doi.org/10.1016/j.commatsci.2022.111601.
[29] Wang V, Xu N, Liu J-C, Tang G, Geng W-T. VASPKIT: a user-friendly interface facilitating high-throughput computing and analysis using VASP code. Comput Phys Commun 2021;267:108033. https://doi.org/10.1016/j.cpc.2021.108033.
[30] Chen X-Q, Niu H, Li D, Li Y. Modeling hardness of polycrystalline materials and bulk metallic glasses. Intermetallics 2011;19:1275–81. https://doi.org/10.1016/j.intermet.2011.03.026.
[31] Li X, Liu H, Du H, Zhang F, Shi J, Hu H, Xie M, Yang L, Dai H. Carbon defect induced evolution of structural and mechanical properties in substoichiometric (HfMoNbZr)Cx films. Tribol Int 2023;190:109034. https://doi.org/10.1016/j.triboint.2023.109034.
[32] Kang J, Liu H, Du H, Shi J, Wang L, Yang L, Dai H. Microstructure, mechanical properties, electrical resistivity, and corrosion behavior of (AlCr)x(HfMoNbZr)1-x

films. Appl Surf Sci 2023;629:157368. https://doi.org/10.1016/j.apsusc.2023.157368.
[33] Kao WH, Su YL, Horng JH, Wu CM. Structure, mechanical properties and thermal stability of nitrogen-doped TaNbSiZrCr high entropy alloy coatings and their application to glass moulding and micro-drills. Surf Coat Technol 2021;405:126539. https://doi.org/10.1016/j.surfcoat.2020.126539.
[34] Tsai D-C, Huang Y-L, Lin S-R, Liang S-C, Shieu F-S. Effect of nitrogen flow ratios on the structure and mechanical properties of (TiVCrZrY)N coatings prepared by reactive magnetron sputtering. Appl Surf Sci 2010;257:1361–7. https://doi.org/10.1016/j.apsusc.2010.08.078.
[35] Tsai C-W, Lai S-W, Cheng K-H, Tsai M-H, Davison A, Tsau C-H, Yeh J-W. Strong amorphization of high-entropy AlBCrSiTi nitride film. Thin Solid Films 2012;520:2613–8. https://doi.org/10.1016/j.tsf.2011.11.025.
[36] Wang Y, Yang Y, Yang H, Zhang M, Qiao J. Effect of nitriding on the tribological properties of Al1.3CoCuFeNi2 high-entropy alloy. J Alloys Compd 2017;725:365–72. https://doi.org/10.1016/j.jallcom.2017.07.132.
[37] Xu Y, Li G, Xia Y. Synthesis and characterization of super-hard AlCrTiVZr high-entropy alloy nitride films deposited by HiPIMS. Appl Surf Sci 2020;523:146529. https://doi.org/10.1016/j.apsusc.2020.146529.
[38] Wang Y, He J, Yan M, Li C, Wang L, Zhou Y. First-principles study of NiAl alloyed with rare earth element Ce. J Mater Sci Technol 2011;27:719–24. https://doi.org/10.1016/S1005-0302(11)60132-1.
[39] Zhang P-X, Ye L, Chen F-H, Han W-J, Wu Y-H, Zhao T. Stability, mechanical, and thermodynamic behaviors of (TiZrHfTaM)C (M = Nb, Mo, W, V, Cr) high-entropy carbide ceramics. J Alloys Compd 2022;903:163868. https://doi.org/10.1016/j.jallcom.2022.163868.
[40] Sun X, Kolawa E, Chen J-S, Reid JS, Nicolet M-A. Properties of reactively sputter-deposited TaN thin films. Thin Solid Films 1993;236:347–51. https://doi.org/10.1016/0040-6090(93)90694-K.
[41] Jauberteau I, Bessaudou A, Mayet R, Cornette J, Jauberteau J, Carles P, Merle-Méjean T. Molybdenum nitride films: crystal structures, synthesis, mechanical, electrical and some other properties. Coatings 2015;5:656–87. https://doi.org/10.3390/coatings5040656.
[42] Inumaru K, Baba K, Yamanaka S. Structural distortion and suppression of superconductivity in stoichiometric B 1 − Mon epitaxial thin films. Phys Rev B 2006;73:052504. https://doi.org/10.1103/PhysRevB.73.052504.
[43] Zheng X, Wang H, Yu X, Feng J, Shen X, Zhang S, Yang R, Zhou X, Xu Y, Yu R, Xiang H, Hu Z, Jin C, Zhang R, Wei S, Han J, Zhao Y, Li H, Wang S. Magnetic origin of phase stability in cubic γ-Mon. Appl Phys Lett 2018;113:221901. https://doi.org/10.1063/1.5048540.
[44] Perry AJ, Baouchi AW, Petersen JH, Pozder SD. Crystal structure of molybdenum nitride films made by reactive cathodic arc evaporation. Surf Coat Technol 1992;(54–55):261–5. https://doi.org/10.1016/S0257-8972(09)90060-3.
[45] Takeuchi A, Inoue A. Classification of bulk metallic glasses by atomic size difference, heat of mixing and period of constituent elements and its application to characterization of the main alloying element. Mater Trans 2005;46:2817–29. https://doi.org/10.2320/matertrans.46.2817.
[46] Lengauer W. Nitrides: transition metal solid-state chemistry. In: Scott RA, editor. Encycl. Inorg. Bioinorg. Chem.. second ed. Wiley; 2015. p. 1–24. https://doi.org/10.1002/9781119951438.eibc0146.pub2.
[47] Pelleg J, Zevin LZ, Lungo S, Croitoru N. Reactive-sputter-deposited TiN films on glass substrates. Thin Solid Films 1991;197:117–28. https://doi.org/10.1016/0040-6090(91)90225-M.
[48] Greene JE, Sundgren J-E, Hultman L, Petrov I, Bergstrom DB. Development of preferred orientation in polycrystalline TiN layers grown by ultrahigh vacuum reactive magnetron sputtering. Appl Phys Lett 1995;67:2928–30. https://doi.org/10.1063/1.114845.
[49] Edalati P, Mohammadi A, Ketabchi M, Edalati K. Microstructure and microhardness of dual-phase high-entropy alloy by high-pressure torsion: twins and stacking faults in FCC and dislocations in BCC. J Alloys Compd 2022;894:162413. https://doi.org/10.1016/j.jallcom.2021.162413.
[50] Fang Q, Chen Y, Li J, Jiang C, Liu B, Liu Y, Liaw PK. Probing the phase transformation and dislocation evolution in dual-phase high-entropy alloys. Int J Plast 2019;114:161–73. https://doi.org/10.1016/j.ijplas.2018.10.014.
[51] Li X, Irving DL, Vitos L. First-principles investigation of the micromechanical properties of fcc-hcp polymorphic high-entropy alloys. Sci Rep 2018;8:11196. https://doi.org/10.1038/s41598-018-29588-z.
[52] Chen Y, Ma J, Lin Y, Hora Y, Zhou Z, Slattery A, An X, Xie Z. Interstitial engineering enabling superior mechanical properties of nitrogen-supersaturated Fe50Mn30Co10Cr10 high-entropy alloys. Acta Mater 2024;277:120214. https://doi.org/10.1016/j.actamat.2024.120214.
[53] Sun J, Li H, Chen Y, An X. Bidirectional phase transformations in multi-principal element alloys: mechanisms, physics, and mechanical property implications. Adv Sci 2024;11:2407283. https://doi.org/10.1002/advs.202407283.
[54] Tan P, Fu L, Teng J, Zhu J, Yang W, Li D, Zhou L. Effect of texture on wear resistance of tantalum nitride film. Tribol Int 2019;133:126–35. https://doi.org/10.1016/j.triboint.2019.01.001.